remote sensing

MDPI

Article

Comparison of Differences in Actual Cropland Evapotranspiration under Two Irrigation Methods Using Satellite-Based Model

Yi Liu [1,2,3], Samuel Ortega-Farías [4], Yunfei Fan [1,2,3], Yu Hou [1,2,3], Sufen Wang [1,2,3,*], Weicai Yang [1,2,3], Sien Li [1,2,3] and Fei Tian [1,2,3]

1 State Key Laboratory of Efficient Utilization of Agricultural Water Resources, Beijing 100083, China
2 National Field Scientific Observation and Research Station on Efficient Water Use of Oasis Agriculture, Wuwei 733009, China
3 Center for Agricultural Water Research in China, China Agricultural University, Beijing 100083, China
4 Research and Extension Center for Irrigation and Agroclimatology (CITRA) and Research Program on Adaptation of Agriculture to Climate Change (A2C2), Faculty of Agricultural Sciences, University of Talca, Talca 3460000, Chile
* Correspondence: wwwsf71@163.com or wangsuf@cau.edu.cn

Abstract: Remote sensing technology is widely used to obtain evapotranspiration (ET_a), but whether it can distinguish the differences in farmland energy balance components and ET_a under different irrigation methods has not been studied. We used Landsat 8 data as the primary dataset to drive the METRIC model and inverted the surface parameters and ET_a of the Shiyang River Basin from 2014 to 2018. After improving the METRIC model using T_a obtained by the regression method instead of interpolation to calculate the net radiation flux (R_n), R^2 was improved from 0.45 to 0.53, and the RMSE was reduced from 61 W/m^2 to 51 W/m^2. The ET_a estimation results on satellite overpass days performed well, with R^2 equal to 0.93 and RMSE equal to 0.48 mm when compared with the Eddy covariance method (EC) observations. Subsequently, the different growth stages and daily average ET_a estimates of maize were compared with three observations (water balance, WB; Bowen ratio and energy balance method, BREB; and EC). The daily estimates of ET_a correlate well with the observations of BREB (R^2_{BI} = 0.82, R^2_{DI} = 0.92; $RMSE_{BI}$ = 0.46 mm/day, $RMSE_{DI}$ = 0.32 mm/day) and EC (R^2_{BI} = 0.85, R^2_{DI} = 0.92; $RMSE_{BI}$ = 0.45 mm/day, $RMSE_{DI}$ = 0.34 mm/day), and the estimation for drip irrigation was found to be better than for border irrigation. The total accuracy of the ET_a estimation on the five-year overpass day of maize farmland reached R^2 = 0.93 and RMSE = 0.48 mm. With sufficient remote sensing data, the 4-year average ET_a of maize was 31 mm lower for DI than for BI, and the mean value of ET_a obtained from the three observation methods was 40 mm. The METRIC model can be used to distinguish ET_a differences between the two irrigation methods in maize farmlands.

Keywords: Landsat 8; METRIC model; cropland; evapotranspiration; irrigation method

Citation: Liu, Y.; Ortega-Farías, S.; Fan, Y.; Hou, Y.; Wang, S.; Yang, W.; Li, S.; Tian, F. Comparison of Differences in Actual Cropland Evapotranspiration under Two Irrigation Methods Using Satellite-Based Model. *Remote Sens.* **2024**, *16*, 175. https://doi.org/10.3390/rs16010175

Academic Editor: Guido D'Urso

Received: 22 November 2023
Revised: 26 December 2023
Accepted: 28 December 2023
Published: 31 December 2023

1. Introduction

Evapotranspiration (*ET*) is the largest outgoing energy flux associated with the water cycle on Earth and is critical for understanding hydrological and ecological processes and the causes of global energy imbalances [1,2]. Farmland is one of the main issues in regional research on climate change and sustainable development and is a hot topic of international concern [3,4]. Water cycle intensification due to climate change can drive dry regions and cause more frequent extreme events, negatively impacting global agricultural production [5–8]. Northwest China is dry and water deficient. Therefore, water consumption for crop growth is mainly dependent on irrigation supply [9]. Ninety percent of agricultural water consumption is used for irrigation [10], almost all of which enters

the atmosphere for evapotranspiration [11,12]. Therefore, it is necessary to map the actual evapotranspiration quantitatively (ET_a) from cropland on a regional scale to understand the distribution and characteristics of agricultural water consumption in arid areas.

The assessment of ET_a is influenced by land cover type, soil moisture, and meteorological conditions [13]. Traditional observation methods of farmland ET_a, such as water balance, micrometeorological methods, and plant physiology methods, provide methods to obtain point-scale ET_a on a uniform surface. However, the extrapolation of point-scale data to larger spatial scales involves biases that are difficult to correct due to the natural dynamics and regional heterogeneity of environmental and surface conditions [2,14–16]. In agricultural and irrigation applications, the crop coefficient method is often used to narrow the range of ET_a to crop evapotranspiration (ET_c) [17]. ET_c is usually obtained by multiplying the reference evapotranspiration (ET_r) by a dimensionless attenuation coefficient known as the crop coefficient (K_c). The ET_r estimation models in the literature can be broadly categorized into (1) full physical models based on the principles of mass and energy conservation, (2) semi-physical models considering the principles of mass and energy conservation, and (3) empirical relational and machine learning black-box-based models [18,19]. ET_r is often calculated from meteorological data using the FAO-56 Penman–Monteith (PM) modeling approach recommended by the Food and Agriculture Organization of the United Nations (FAO) [20]. K_c can be determined based on the crop type and stage of growth and is subject to variations caused by different environmental conditions [21,22]. However, it is unclear whether the actual crop type and growth conditions are consistent with those represented by idealized K_c values in arid regions. In addition, the application of the K_c method over large areas can be limited by its inability to determine the growth stages of multiple crops [23,24]. With the rise of intelligent algorithms and remote sensing technology, which has large-capacity and large-scale data collection characteristics, high spatial and temporal resolution Earth observation data can be calculated to map the spatiotemporal changes in ET_a [22,24,25].

Evapotranspiration can be estimated using two or more consecutive satellite images that provide the spatial distribution of the required factors, regardless of soil conditions, crops, and farm management [26]. Remote sensing evapotranspiration models can be classified into two categories, single-source and dual-source, depending on the residual energy balance theory for the soil–plant–atmosphere interface [27,28]. The single-source model treats soil and crop vegetation as a whole, whereas the dual-source model separates soil and vegetation based on vegetation indices [29]. Both types of models generally estimate the latent heat flux (LE) from the residual term of each image pixel, which is obtained using net surface radiation (R_n) minus soil heat flux (G) and sensible heat flux (H) [25,30]. When the auxiliary data are sparse, the single-source model can provide higher accuracy than the dual-source model because it requires less parameter input [28,29].

Allen et al. [31] proposed mapping evapotranspiration at a high resolution with an internalized calibration (METRIC) model based on the Surface Energy Balance Algorithm for Land (SEBAL) model [32]. The METRIC model has several advantages and improvements over other single-source models.(1) This model redefines the rules for estimating H under extremely cold and hot conditions by introducing ET_r as a ground reference. (2) The model considers elevation, convection, and wind speed and also improves the application of the model in areas with large terrain fluctuations and the extension method of instantaneous ET [33–35]. (3) In the METRIC model, the linear relationship between the near-surface temperature gradient (dT) and surface temperature (T_s) was calibrated using the inverse model under an extreme condition (CIMEC) process and theoretically defined extreme hydrological conditions (cold, hot), eliminating the need to map H with air temperature (T_a) within the modeling domain. Furthermore, the CIMEC process excludes potential biases related to surface energy balance components (SEBCs), radiometric corrections, and model assumptions [33]. (4) Initially, the METRIC model was designed for Landsat satellite imagery to maximize the accuracy of evapotranspiration estimates [28]. (5) Globally, this model has been successfully implemented in multiple irrigated agricultural areas and

is considered effective for providing spatially distributed *ET* [36]. Current research has focused on the development of ET_a estimation tools that use simpler platforms to improve the range of model use and estimation accuracy [37].

Ensuring high-quality and sustainable development of agricultural water use is necessary to solve the main problem of water use in the Shiyang River Basin in the arid area of northwest China. Maize is a widely distributed crop that adapts to the local climate. Border irrigation (BI) is still widely used as a traditional irrigation method in corn farmlands in northwest China. Compared with drip irrigation (DI), BI results in high soil evaporation and lower irrigation water use efficiency [38]. With the development and promotion of water-saving technology, many studies have compared the impacts of the two irrigation methods. Previous studies have proved that DI can accelerate the growth of maize and reduce water consumption [39]. The accuracy of remote sensing technology for obtaining ET_a has been verified in many cases. However, can remote sensing technology detect ET_a differences caused by different irrigation methods in maize croplands?

Therefore, the METRIC model was coded on the Google Earth Engine (GEE) platform to estimate various surface parameters using Landsat 8 images as the primary data source in this study. After the accuracy of the instantaneous surface energy fluxes was verified, the SEBCs of maize farmlands under BI and DI were compared. In addition, the accuracy of the ET_a estimation at the satellite overpass days and at each growth stage obtained from the METRIC model was verified. Finally, the ability of remote sensing to discriminate differences in ET_a in maize farmlands under different irrigation methods was assessed. This study provides a basis for determining whether satellite remote sensing can be utilized to accurately monitor farmland in the future.

2. Materials and Methods

2.1. Study Area

The Shiyang River basin is located in the arid region of northwest China, with a coordinate range of 101°40′–104°20′E and 36°30′–39°30′N, an area of 41,600 km^2, and an altitude of 1244–5220 m (Figure 1). The landscape is a complex mountain–oasis–desert ecosystem, of which approximately 10% is oasis farmland. The basin has a temperate, arid continental climate with abundant light and heat resources, an annual sunshine time of 3028 h, and a frost-free period of more than 150 days, which is suitable for the growth of commercial crops [40]. However, the average annual precipitation is less than 200 mm, the evaporation of the pan is 2000 mm, and the average depth of groundwater is 25 m. Because the water demand for local crops is much higher than precipitation, farmlands must be irrigated with surface water and groundwater as the main water source.

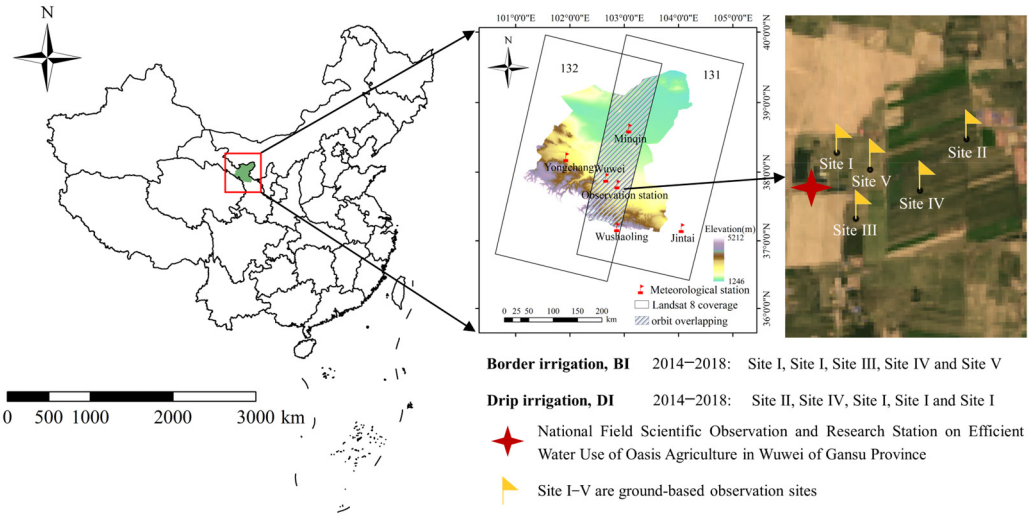

Figure 1. Overview of the study area and description of the observation sites.

2.2. Remote Sensing, Auxiliary Data, and Data Processing

The Landsat 8 satellite is equipped with two sensors: OLI and TIRS. The OLI land image includes nine bands, including a 15 m panchromatic band. The other bands have a spatial resolution of 30 m and an imaging width of 185 km. The resolution of the two thermal infrared bands of the TIRS is 100 m, which helps to distinguish and calculate the surface and atmospheric temperature. This study used four Landsat 8 images covering the entire study area, numbered 131/033, 131/034, and 132/033, 132/034 (Figure 1). Unfortunately, there are only five meteorological stations in and around the study area that can provide relevant data.

Google Earth Engine (GEE) (https://earthengine.google.com/ (accessed on 25 December 2023)), a cloud computing-based geospatial processing platform, uses Google's computing infrastructure for rapid analysis [41]. Almost all built-in algorithms of the platform use pixel-by-pixel computing, which can efficiently process and mine remote sensing data globally. This study used the online JavaScript API of the GEE platform to invoke and analyze Landsat 8 raw and surface reflectance product (SR) datasets from public catalogs and Landsat 8 images courtesy of the U.S. Geological Survey. Images with less than 30% clouds from 2014 to 2018 were efficiently selected, cloud removed, stitched, cropped, subjected to parameter inversion, and interpolated for meteorological data. The METRIC model was encoded and processed on the platform, and the model process is illustrated in Figure 2. The model only outputs the *ET* inversion results, significantly improving computational efficiency.

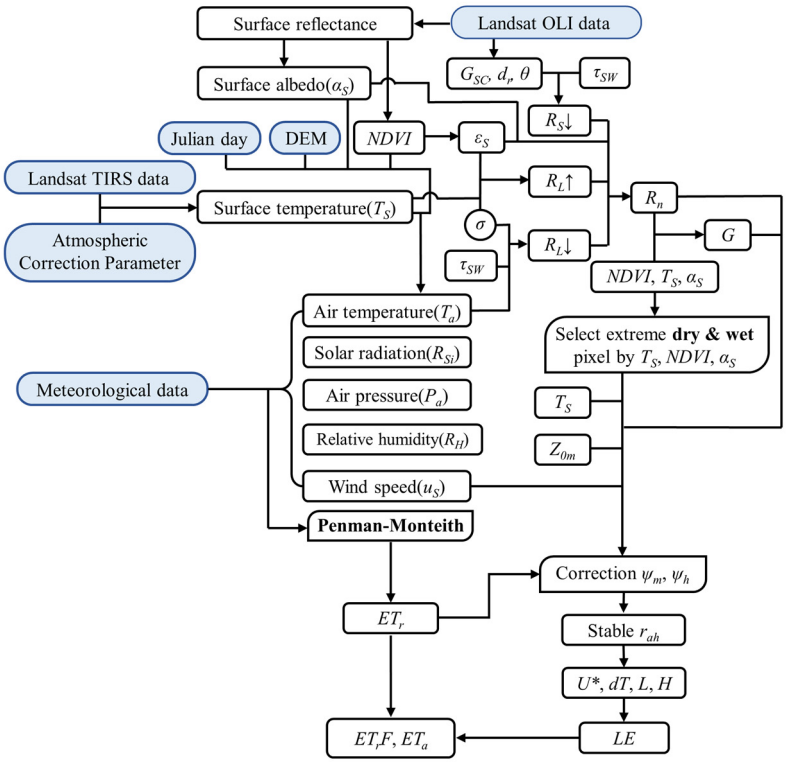

Figure 2. Flowchart of the METRIC model.

2.3. In Situ Dataset

Observations of ET_a and energy fluxes were obtained from seed maize fields in and near the National Field Scientific Observation and Research Station on Efficient Water Use of Oasis Agriculture in Wuwei, Gansu Province. The maize farmlands used for the observations were not fixed because of local adjustments in field production. These locations are shown in Figure 1. In 2014–2018, the flux/ET_a locations of the BI observation areas were at Site I, Site I, Site III, Site IV, and Site V, respectively, and the flux/ET_a locations

of the DI observation area were at Site II, Site IV, Site I, Site I, and Site I, respectively (see Table 1 for field information) [38].

Table 1. Different field management information, surface energy flux observation locations, and the number of remote sensing images.

Crop	Irrigation Method	Years	Site	Area	Growth Period Days	Number of Remote Sensing Images	Observation Method
seed maize	border irrigation under mulch field	2014	I	400 m × 200 m	149	8	Water balance method; Bowen ratio and energy balance method; Eddy covariance method
		2015	I		155	6	
		2016	III		154	7	
		2017	IV	500 m × 250 m	147	6	
		2018	V		159	8	
	drip irrigation under mulch field	2014	II	2000 m × 1000 m	134	8	
		2015	IV	500 m × 250 m	132	6	
		2016	I		144	7	
		2017	I	400 m × 200 m	142	5	
		2018	I		146	8	

In this study, the eddy covariance (EC), Bowen ratio energy balance (BREB), and soil water balance (WB) methods were used to systematically compare and observe the components of water–heat fluxes in seed maize fields under mulched border irrigation and drip irrigation under membrane over the whole growth stage, respectively.

The EC system mainly consists of a three-dimensional sonic anemometer/thermometer (model CSAT3, Campbell Scientific, Inc., Logan, UT, USA), a Krypton hygrometer (model KH20)/an open path gas analyzer (model EC150, Campbell Scientific, Inc., USA), a temperature and humidity sensor (model HMP45C/HMP155A, Vaisala, Vantaa, Finland), an infrared radiometer (model SI-111, Campbell Scientific, Inc., USA), a net radiometer (model NR-LITE/CNR4, Kipp & Zonen, Delft, the Netherlands), two soil heat flux plates (model HFP01, Hukseflux, the Netherlands), and a date logger (model CR1000/CR3000/CR5000, Campbell Scientific, Inc., USA) [39,42]. The installation height was 4 m above ground level in 2014 and 2016–2018 and 3.5 m above ground level in 2015. The net radiometer and surface temperature sensors were installed at the same height as the three-dimensional sonic anemometer/thermometer. Two soil heat flux plates were buried 5cm below the surface of the mulched soil and the bare ground between the mulches, respectively. All sensors were located in the BI and DI observation areas and were connected to a data logger, and the system sampled at a frequency of 10 Hz and output energy flux data every 30 min. The systems are all installed in the middle of a flat and open observing area, which meets the requirements of the EC system for wind and wave areas [43].

The Bowen ratio energy balance method is based on the energy balance equation and the diffusion theory of near-surface gradients to estimate *LE* and *H* [44]. BREB measurements require two temperature and relative humidity probes (model HMP155A, Vaisala, Vantaa, Finland) at different heights to monitor the gradient of temperature and humidity. There are also probes that can be shared with the EC system, such as a radiometer and soil heat flux panels.

In addition, soil moisture probes (model CS616, Campbell Scientific, Inc., USA) were installed at 20 cm, 40 cm, 60 cm, 80 cm, and 100 cm below the soil surface to monitor soil moisture changes, which can be used in WB methods.

The collected EC flux data were processed using Eddy Pro 4.0 software, and then the quality of the EC data was assessed. Data that were unreliable and out of experimental range were removed. Linear interpolation was used to fill in data gaps when fewer than four consecutive observations were missing, and MDV (mean daily variation) was used when five or more observations were missing. For the BERB flux data, the data were

corrected using the directivity judgment method and the rejective region method [45]. The method for filling data gaps was the same as that used for EC flux data [39].

The EC technique is recognized as the standard micrometeorological method for measuring *ET* because of its high measurement accuracy and sampling frequency. This technique can accurately obtain *ET* information over a wide range of scales [23,46] and has become the primary method of the International Flux Observation Network (FLUXNET) [47]. The instantaneous flux data of the EC system in 2014–2015 were utilized to validate the remote sensing data retrieval of the satellite transit time.

3. Surface Parameters Determination

When satellite remote sensing data are acquired for ET_a, the energy information of the soil, vegetation, and atmosphere, as well as other characteristic parameters, must first be obtained through image processing techniques [48].

3.1. Surface Parameters

This study used datasets (atmosphere and surface reflectance products) in the GEE platform to invert the surface temperature of the study area based on the atmospheric correction method. The radiative transfer equation of the thermal infrared radiance value L_λ received by the satellite sensor is expressed as follows [49]:

$$L_\lambda = [\varepsilon B(T_s) + (1-\varepsilon)L\downarrow]\tau + L\uparrow \quad (1)$$

where L_λ is the spectral radiance value at the top of the atmosphere at the band λ ($W{\cdot}m^{-2}{\cdot}\mu m^{-1}{\cdot}sr^{-1}$), ε is the surface-specific emissivity, $B(T_s)$ is the blackbody thermal emissivity brightness ($W{\cdot}m^{-2}{\cdot}\mu m^{-1}{\cdot}sr^{-1}$), $L\downarrow$ is the downward radiance of the atmosphere after reflection on the ground ($W{\cdot}m^{-2}{\cdot}\mu m^{-1}{\cdot}sr^{-1}$), τ is the atmospheric thermal infrared band transmittance, and $L\uparrow$ is the upward radiance of the atmosphere ($W{\cdot}m^{-2}{\cdot}\mu m^{-1}{\cdot}sr^{-1}$).

Thermal infrared radiance values were provided by the 10th band of the Landsat 8 image, and the formula for calculating $B(T_s)$ is:

$$B(T_s) = \frac{[L_\lambda - L\uparrow - (1-\varepsilon)\tau L\downarrow]}{\tau\varepsilon} \quad (2)$$

$$T_s = \frac{K_2}{\ln\left(\frac{K_1}{B(T_s)} + 1\right)} \quad (3)$$

where T_s is the surface temperature (°C), $K_1 = 774.89\ W{\cdot}m^{-2}{\cdot}\mu m^{-1}{\cdot}sr^{-1}$, $K_2 = 1321.08$ K.

For areas with a sparse and uneven distribution of meteorological stations, the extended results of interpolating the T_a data of meteorological stations on a regional scale are affected by the heterogeneity of the surface [50]. Meanwhile, the atmospheric radiation value caused by T_a cannot be obtained directly from satellite images due to its complex proportion and low total amount. Using the surface parameters obtained from remote sensing inversion to establish a regression relationship with meteorological station data, regional T_a data were obtained. The regression algorithm for calculating T_a was established by Liu et al. [51]:

$$T_a = b_0 + b_1 T_s + b_2\alpha + b_3 NDVI + b_4 A + b_5 x7 + b_6 x8 \quad (4)$$

where T_a is the near-surface air temperature, T_s is the surface temperature, α is the surface albedo, *NDVI* is the normalized difference vegetation index, A is the altitude, $x7 = (J-200)^2$ is the independent variable, and J is the Julian day. T_s and J are independent variables and have a strong correlation. Therefore, $x8 = x7 \times T_s$ is used as the interaction term to match the model, and $b_0 \sim b_6$ are undetermined coefficients.

For latent heat estimation, the meteorological data and physiological characteristics of the vegetation structure (vegetation index and vegetation coverage) are indispensable for describing the atmospheric boundary layer. Point-scale wind speeds from five surface meteorological stations (http://data.cma.cn/ (accessed on 25 December 2023)) in and around the basin were interpolated and expanded using inverse distance weighting (IDW).

Surface reflectance (α) is the ratio of reflected solar radiation to incident solar radiation in the short-wave spectrum (0.2–3.2 μm) [33]. Flood [52] compared the surface albedo calculated by Landsat 8 OLI and Landsat 7 ETM+. The surface albedo results calculated by these two sensors were highly consistent. Therefore, after application comparison, the parameters given by Liang [53] for Landsat 7 were used:

$$\alpha = 0.356b_2 + 0.130b_4 + 0.373b_5 + 0.085b_6 + 0.072b_7 - 0.0018 \quad (5)$$

where α is the broadband surface reflectance; b_2, b_4, b_5, b_6, and b_7 are the surface reflectance of subscripted bands, respectively.

3.2. METRIC Model

Based on the surface energy balance principle (Equation (6)), the METRIC model obtains the latent heat flux (LE) after determining the other three instantaneous energy components and converts it into instantaneous ET_a. Based on the available Landsat 8 images, the METRIC model was used to estimate the ET_a in the Shiyang River Basin.

$$\lambda ET_{inst} = LE = R_n - G + H \quad (6)$$

$$R_n = (1 - \alpha)R_S - R_L \uparrow + \varepsilon_s R_L \downarrow \quad (7)$$

$$R_S = G_{SC} \times d_r \times \tau_{sw} \times cos\theta \quad (8)$$

$$R_L \uparrow = \varepsilon \times {T_S}^4 \times \sigma \quad (9)$$

$$R_L \downarrow = 1.08 \times (-ln\tau_{sw})^{0.265} \times {T_a}^4 \times \sigma \quad (10)$$

$$\tau_{sw} = 0.75 + 2 \times 10^{-5} \times z \quad (11)$$

To represent relatively homogeneous atmospheric conditions within a region, the METRIC model assumes that the T_a of the calculated region is consistent with the T_s of the cold spots [54]. However, the study area is an alpine alpine–desert–oasis ecosystem, with large differences in vegetation types and a high proportion of desert areas. In particular, T_s varies considerably across land cover types when the ground surface is dry [55]. Therefore, the assumptions of the METRIC model for calculating $R_L \downarrow$ do not apply to this region. Further comparison of the differences in R_n estimation accuracy between the two methods of estimating T_a is required. According to the calculation formula above for R_n, the T_a obtained in two distinct ways is substituted into the R_n calculation. The results were verified using instantaneous flux observation data corresponding to satellite overpass days in 2014–2015 (the overpass time of Landsat 8 was local from 11:43 to 11:49 a.m.).

Soil heat flux (G) refers to the energy stored in soil and vegetation. G was used to estimate the available energy ($R_n - G$), which can be divided into H and LE [28]. We have tried to avoid introducing more parameters from empirical formulas while better representing complex surface conditions and vegetation changes [32]. In this study, the estimation method proposed by Bastiaanssen [56] was used to obtain G:

$$G = \frac{(T_s - 273.15)}{\alpha}(0.0038\alpha + 0.0074\alpha^2)(1 - 0.98NDVI^4)R_n \quad (12)$$

Sensible heat flux (H) was estimated from the aerodynamic function:

$$H = \frac{\rho_{air} C_p dT}{r_{ah}} \quad (13)$$

There are two unknown variables (dT and r_{ah}) in Equation (13), making it challenging to obtain H. Therefore, the algorithm needs to determine the two extreme pixels (hot and cold pixels) and then compute dT and r_{ah} by a trial-and-error method during the iteration process. There are many studies describing the computation of H, which will not be repeated here [31,33]. The process is shown in Figure 2, where the selection of hot and cold pixels is crucial for the estimation of H.

The METRIC model assumes that the hot pixels are dry, hot, and bare soil without vegetation, so $LE_{hot} = 0.05 \times \lambda \times ET_{r\_hourly}$, $H_{hot} = R_{n\_hot} - G_{hot} - LE_{hot}$. In contrast, the cold pixels are saturated with vegetation and have excellent water supply conditions, so $LE_{cold} = 1.05 \times \lambda \times ET_{r\_hourly}$, $H_{cold} = R_{n\_cold} - G_{cold} - LE_{cold}$ [33].

When selecting extreme pixels, it is necessary to refer to the NDVI, α, and T_s simultaneously. The pixels with NDVI less than 0.1 and the hottest 20% of T_s were regarded as hot pixels. "Ideal candidate cold pixels" recommend α in the range of 0.18–0.25, with low T_s and NDVI in the range greater than 0.8. Generally, after the cold pixels meet the α range, the first 5% larger NDVI is selected, and the pixels with the lowest 20% T_s were determined as the cold pixels. If there are no suitable pixels, the α range can be adjusted by $\pm$ 0.02 [34].

Through the latent heat of the water vaporization parameter, instantaneous surface evapotranspiration ($ET_{overpass}$) was obtained. Then, we calculated the reference evapotranspiration fraction (ET_rF) combined with the instantaneous reference evapotranspiration (ET_r). The instantaneous reference evapotranspiration ($ET_{rhourly}$) was calculated with reference to the sinusoidal variation curve of evapotranspiration in sunny days by Equation (16). It is assumed that the ET_rF does not change within a day, and the mean value of the satellite overpass days is the same as the value of the satellite overpass time.

$$ET_{overpass} = 3600 \times \frac{LE}{\lambda} \tag{14}$$

$$\lambda = (2.501 - 0.00236 \times (T_s - 273)) \times 10^6 \tag{15}$$

$$ET_{r_{hourly}} = \frac{ET_{r_{daily}} \times \pi \times \sin\left(\frac{\pi t}{N-2}\right)}{2(N-2)} \tag{16}$$

$$ET_rF = \frac{ET_{overpass}}{ET_{r_{hourly}}} \tag{17}$$

$$ET_{daily} = ET_rF \times ET_{r_{daily}} \tag{18}$$

In regions with different seasons, ideal vegetation conditions are not always available or provide cold pixels. Therefore, in the non-growing period when no well-growing crops completely cover the ground, the selection range of the cold pixels must be adjusted appropriately. When the NDVI of cold pixels is lower than 0.75, the ET_rF_{Cold} can be adjusted to less than 1.05 [54,57]. Normally, hot pixels lack water for evaporation, but ET_rF_{Hot} can be adjusted to be greater than 0.05 if rainfall results in soil evaporation residuals [34]. The transport of water vapor and H on Earth's land surface is strongly influenced by aerodynamic processes, including wind speed, turbulence, and buoyancy, but all of these are difficult to determine for satellites. In addition, surface albedo, Rn, and G cannot be quantified with complete precision. Therefore, despite the best efforts to estimate each parameter accurately, some bias can still occur. The introduction of ET_r calibration in the METRIC model helps to compensate for this bias by introducing a bias correction in the H calculation. Ultimately, the inherent bias in the Rn, G, and H subcomponents was eliminated by subtracting the bias in H.

Landsat 8 provides optical remote sensing data and is susceptible to cloudy weather with long overpass revisit times. Therefore, the METRIC model, which assumes a constant ET_rF, is used to estimate ET_a for dates near the satellite overpass date [29]. We used the cubic B-spline method to simulate the ET_rF profile of maize during growth. Many researchers have used the cubic B-spline method to determine numerical schemes for solving boundary value problems because of their flexibility and reliability in finding

an approximate solution at any occasion in the domain [58]. The ET_{total} formula for the corresponding crop growth period is as follows:

$$ET_{total} = \sum_{i=1}^{n} ET_{daily_i} \tag{19}$$

Appendix A lists the meanings and units of the parameters used in Equations (6)–(19).

3.3. Coding and Validation of the METRIC Model

We applied JAVA programming to the METRIC model shown in Figure 2, which can directly use the remote sensing dataset and the powerful pixel-by-pixel computing capability provided by the GEE platform. The main processes include image filtering, stitching, clipping, surface temperature, and other parameter operations. The operation process has two points that require special attention: (1) after restricting the conditions of NDVI, T_s, and α in the study area, the code selects the eligible areas autonomously and then subsequently makes manual judgments and selections; (2) the momentum transport stabilizing factors (ψ_m) and the heat transport stabilizing factors (ψ_h) are introduced, and the air density (ρ_{air}) and aerodynamic resistance (r_{ah}) are operated for several iterations to obtain stable H values. The technical route to indicate the overall flow of the study is shown in Figure 3.

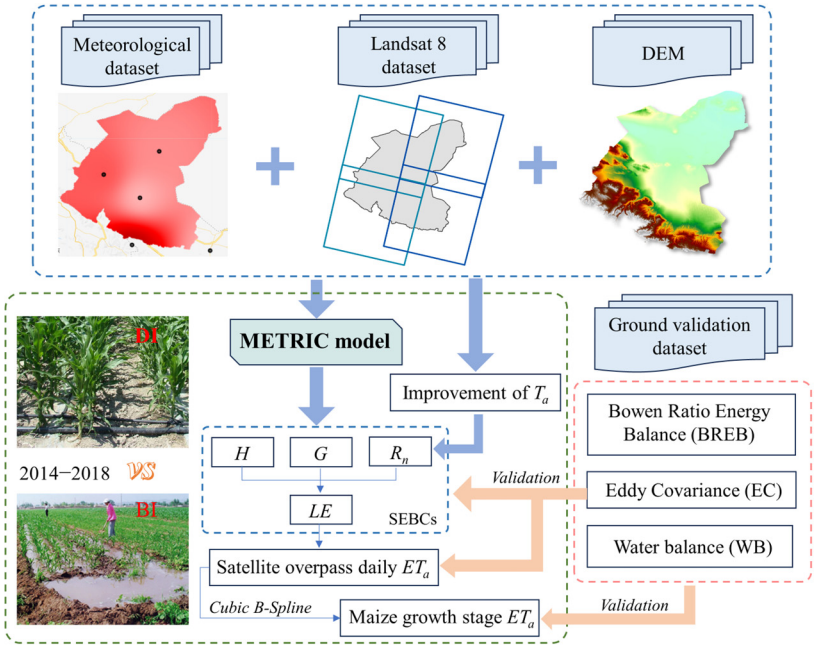

Figure 3. Flow chart of the research.

The energy balance components and the ET_a of the model output were validated against the corresponding observations. The EBC was validated using instantaneous data, and the ET_a was validated using daily and growth stage observations. The coefficient of determination (R^2), root mean square error (RMSE), and bias were used to understand the agreement between the model estimates and in situ datasets.

$$R^2 = \frac{\sum_{i=1}^{N}(y_i - \overline{O})^2}{\sum_{i=1}^{N}(O_i - \overline{O})^2} \tag{20}$$

$$\mathrm{RMSE} = \left(\frac{1}{N}\sum_{i=1}^{N}(y_i - O_i)^2\right)^{\frac{1}{2}} \tag{21}$$

$$\text{Bias} = \frac{1}{N}\sum_{i=1}^{N}(O_i - y_i) \quad (22)$$

where N is the number of dates (days), y_i is the estimation of EBC or ET_a at the ith day using the METRIC model, O_i is the measured value of the corresponding day, and $\overline{O}$ is the average value of the measured values.

4. Results and Discussion

4.1. Inversion Accuracy of Energy Fluxes

The average T_a data obtained using the regression model (described in Section 3.1 Surface parameters) were more conducive to calculating the instantaneous R_n (Figure 4a) compared with T_a from meteorological data. Although the overall estimated results were higher than the observed value, the R^2 increased from 0.45 to 0.53, the RMSE decreased from 60.76 to 50.85 W/m^2, and the bias increased from −29.24 to −16.66 W/m^2. This improvement can be attributed to the fact that the data interpolated from the weather station are much higher than the actual T_a data of the farmland, and the temperature data obtained by the regression model are more in line with the practical situation.

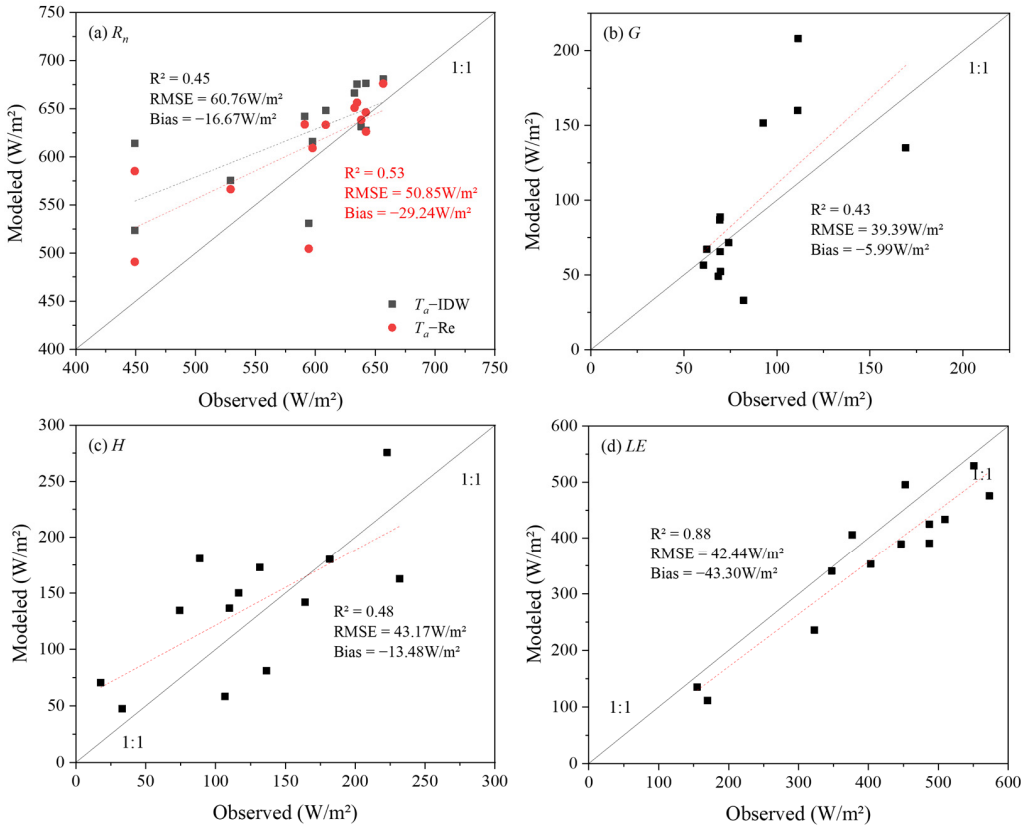

Figure 4. Plot of flux component results from METRIC model estimation against EC observations. (**a**) net surface radiation (R_n), (**b**) soil heat flux (G), (**c**) sensible heat flux (H), and (**d**) latent heat flux (LE). R^2 is the coefficient of determination. RMSE is the root mean square error (W/m^2).

The verification results of G were similar to those of the R_n verification. The estimated G showed that the R^2 was only 0.43, but its RMSE value was 39.39 W/m², and the bias was −5.99 W/m² (Figure 4b). High G values indicate that the soil absorbs more heat when the surface energy fluctuates significantly and is prone to error. The surface temperatures of different land cover types are quite different when the ground surface is in a spanking dry state, affecting the dT and H estimations of each pixel.

The instantaneous LE was derived as the residual term of the energy balance equation (Equation (6)). Most of the points in the scatter plot (Figure 4d) after validation were close to

the 1:1 line, and the estimated values were slightly lower than the observed values; the R^2, RMSE, and bias were 0.88, 42.44 W/m^2, and 43.30 W/m^2, respectively. Furthermore, *LE* was less affected by the errors of the other fluxes, and its estimation accuracy was superior to that of all other flux components. These results are related to the kernel of the METRIC model, which utilizes internal self-calibration (inverse modeling at extreme conditions, CIMEC) to remove the effects of biases associated with surface reflectance, temperature, and estimations of *G* and *H* [54,55]. Oliveira et al. [59] used the METRIC model to estimate the surface energy balance components for three landscapes (sugarcane, woody savanna, and stricto-sensu savanna) in the Brazilian Cerrado, where the *LE* estimation accuracy for sugarcane was the best (RMSE = 21.43W/m^2, R^2 = 0.94) and the *LE* estimation accuracy was the lowest for woody savanna (RMSE = 56.38W/m^2, R^2 = 0.93). Carrasco-Benavides et al. [60] estimated *H* and *LE* in vineyards with RMSE in the range of 35–48 W/m^2 using METRIC models at the time of satellite overpass. Ortega-salazar et al. [55] estimated *H* and *LE* in olive groves below the observed values (RMSEs of 46 and 45 W/m^2, respectively), obtaining similar results to those of this study. Feng et al. [61] used an optimized two-source energy balance (TSEB) model to estimate *LE* for maize farmland in the Heihe River Basin, with an RMSE = 85 W/m^2. Ge et al. [62] used the SEBS model to estimate the energy balance components of alpine and subalpine meadow on the northern Tibetan Plateau ($RMSE_H$ = 68.2 W/m^2 and $RMSE_{LE}$ = 54.9 W/m^2).

Proper selection of hot and cold pixels can correctly partition the available energy ($R_n - G$) into *H* and *LE*, which will improve the accuracy of *LE*. Therefore, the performance of the METRIC model in the final *LE* estimation indicates the applicability of extreme point selection conditions in the study area. The Landsat 8 satellite has a long revisit, and the ground-based flux observations were made only during the maize growth period. Just in case two years of verifiable flux data were not sufficient, we used five years of model-derived flux data to compare with measured leaf area index (*LAI*) to further analyze the reliability of the METRIC model.

The flux data of *H* and *LE* under the two irrigation methods from 2014 to 2018 were compared and analyzed concerning the trends and differences in the measured *LAI* data (Figure 5). In standard years (except for 2017), maize under the DI method grew better than BI, with $LAI_{DI} > LAI_{BI}$ in the early and middle stages of the growth process, while there were more cases of higher values of LE_{DI}. In 2017, maize under the DI treatment was more affected by the rust disaster and did not grow as well as in standard years, so $LE_{BI} > LE_{DI}$ on most dates. Although $LE_{BI} > LE_{DI}$ on July 22 and 7 August 2016, the difference was not large, both were less than 6%, and the $H_{BI} > H_{DI}$ of the two dates was similar to that in other years. After 21 July 2018, the maize *LAI* of DI was still greater than that of BI, but the *LAI* of DI had an obvious downward trend and aging was rapid, so the value of *LE* was small. The comparison concluded that *LE* was correlated with *LAI* in maize farmland (Figure 6), which is a convergent saturation process, and the R^2 of the quadratic fitted curve for *LE-LAI* was higher under DI (R^2_{DM} = 0.89, R^2_{BM} = 0.77). This is similar to other biophysical variables being related to *LAI* due mainly to the attenuation and absorption exponential process of radiation as the layers of vegetation increase [63]. The overall difference in *H* under the different irrigation methods was pronounced, and $H_{BI} > H_{DI}$ was more frequent (71.4%), except in 2017. Therefore, the *H* was lower in the maize farmland under the DI treatment at the midday moment on a clear day when satellite data were available. The above demonstrates that the allocation of R_n to seed maize farmland under the DI method is biased towards *LE*, leading to higher ET_a on transit days, which would promote maize growth.

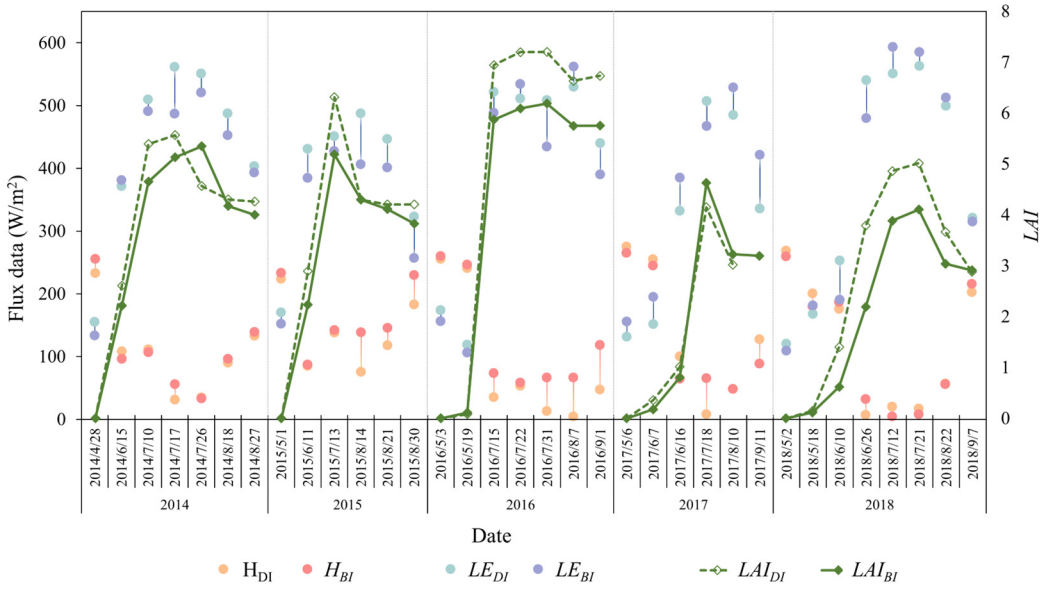

Figure 5. Sensible heat flux (*H*), latent heat flux (*LE*), and measured leaf area index (*LAI*) estimates of maize under two irrigation methods at Landsat 8 overpass days from 2014 to 2018. DI is the drip irrigation method. BI is the border irrigation method.

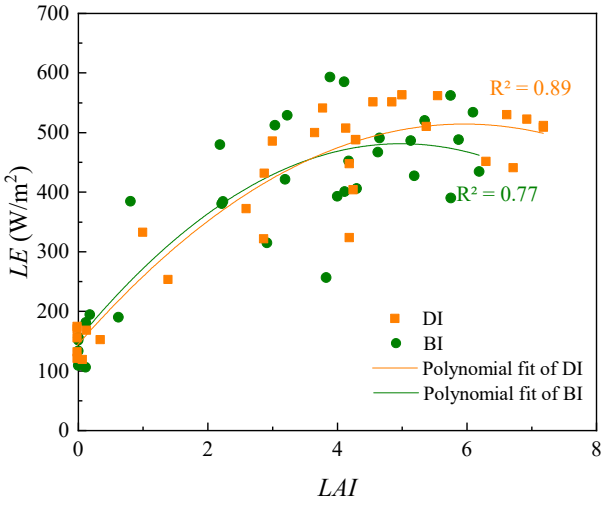

Figure 6. Plot of *LE* results from METRIC model estimation against *LAI* observations from 2014 to 2018. DI is the drip irrigation method. BI is the border irrigation method.

4.2. Satellite Overpass Daily ET_a Validation

With a reasonable selection of hot and cold pixels, the correct division of *H* and *LE* improves the accuracy of the *LE*. Validation of the flux data showed that the surface parameters and selection of extreme points in the model were applied to the study area. Furthermore, we estimated ET_a during the growth period of the maize seed. Observation data obtained from EC systems at four different locations and years were used to validate the ET_a obtained from remote sensing data for different crops and irrigation methods from 2014 to 2018.

The instantaneous *LE* values were converted to the moment ET_a of overpass and then extended to the daily value. This step is essentially an extension of the reference evapotranspiration ratio, assuming that ET_rF remains constant on the day of the satellite overpass. For comparison, we extracted the estimated values of ET_a under different irrigation methods for seed maize production and plotted them against with ET_r (Figure 7a–e). As the maize grew, ET_a, ET_r, and their ratio ET_rF changed, showing an increasing and then

decreasing trend. At the early stage of maize growth, ET_a under both irrigation methods is much lower than ET_r, with $ET_rF < 1.0$. With the arrival of the peak growth stage in July and August, ET_a is larger than ET_r, with $ET_rF > 1.0$. Before the end of the reproductive period, the difference between ET_a and ET_r values was smaller.

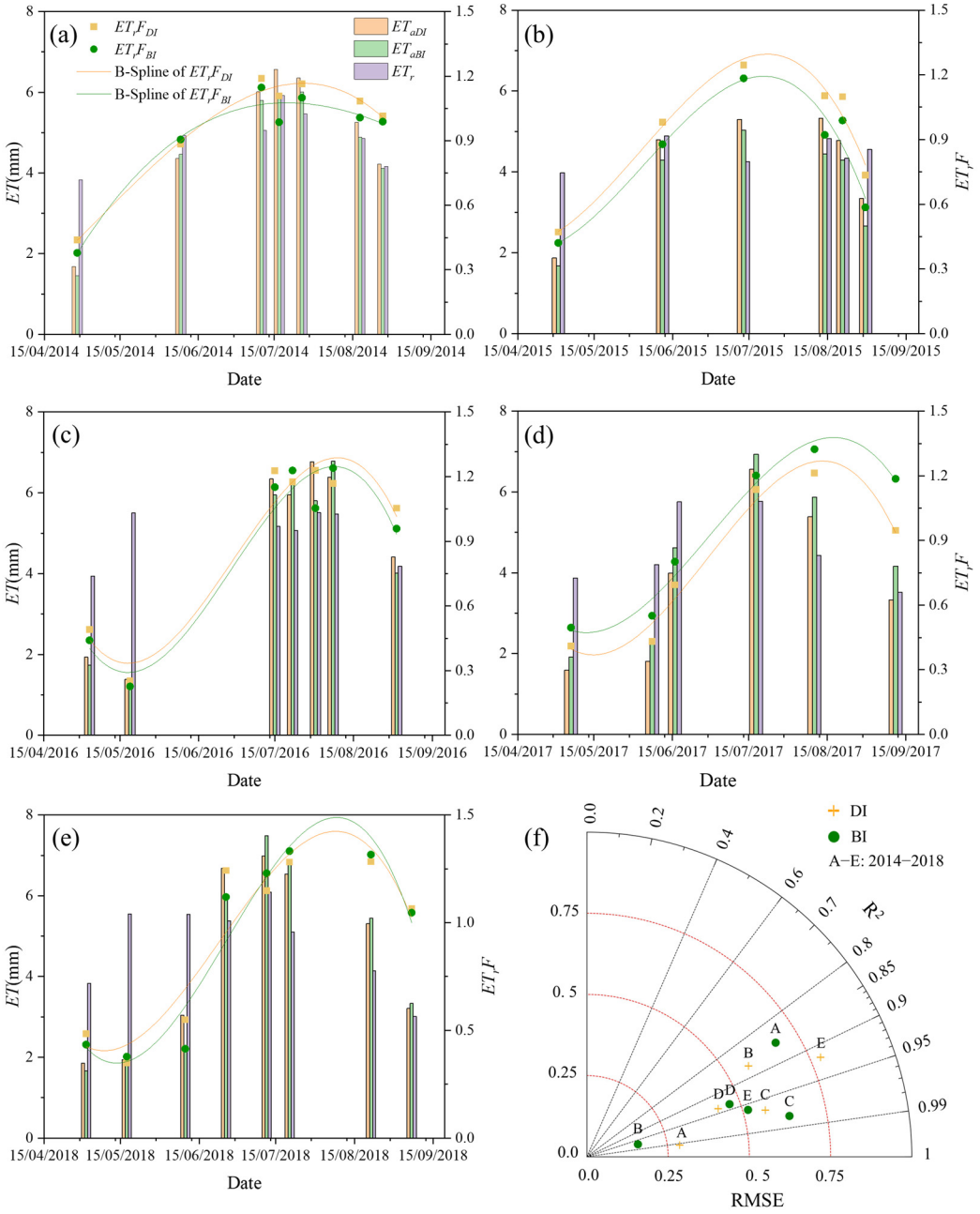

Figure 7. Estimations of ET_a, ET_rF, and time-expanded curves (**a**–**e**) with accuracy performance (**f**) for maize under two irrigation methods at Landsat 8 overpass days, 2014–2018. ET_a (mm/day) and ET_r (mm/day) are daily actual and reference evapotranspiration, respectively. ET_rF is the reference evapotranspiration fraction. DI is the drip irrigation method. BI is the border irrigation method. R^2 is is the coefficient of determination. RMSE is the root mean square error (mm/day).

The METRIC model had the highest goodness of fit for the estimation of ET_a under the DI treatment in 2014, with $R^2 = 0.99$; however, in the same year, the BI treatment had the lowest R^2, with $R^2 = 0.85$, whereas the estimation with the smallest value of bias was that of the BI in 2015, with RMSE = 0.16 mm/day, and that of the DI in 2018 had the largest

bias value, with RMSE = 0.78 mm/day (Figure 7f). Overall, the accuracy of the daily ET_a of maize obtained from the estimation was high.

This study required long-term baseline observations of large areas of agricultural land, which were used to fully validate the low-temporal-resolution Landsat remote sensing images. Therefore, we used five years of measured data to validate the accuracy of the remote sensing model in estimating ET_a in agricultural fields. The results of some studies are similar to those we found, suggesting that the METRIC model performs well in farmland evapotranspiration inversion. For example, Nisa et al. [37] used three models based on Landsat 7 data to estimate daily ET_a from fennel/maize/ryegrass clover cropland rotations in a Mediterranean context in southern Italy and found that the SEBS and METRIC models performed well (R^2 = 0.59, RMSE = 0.71 mm/day; R^2 = 0.65, RMSE = 1.13 mm/day). Kamyab et al. [64] used the SEBAL and METRIC models to map ET_a on maize farmland in Iran, and the results showed a higher correlation and smaller RMSE for METRIC estimates than for SEBAL estimates (R^2 = 0.885, 0.793; RMSE = 0.711 mm/day, 1.046 mm/day). Xue et al. [65] estimated daily ET_a for maize using three remote sensing evapotranspiration models, METRIC, pySEBAL, and SEBS, and found that all of them overestimated ET_a, among which SEBS performed better (R^2 = 0.74, RMSE = 1.0 mm/day) than pySEBAL (R^2 = 0.72, RMSE = 1.08 mm/day) and METRIC (R^2 = 0.78, RMSE = 1.2 mm/day). Reyes-gonz et al. [66] used the METRIC model to estimate ET_a for a commercial maize farmland and compared it to field measurements, with a high coefficient of determination (R^2 = 0.89) and low RMSE (0.71 = mm/day). Comparisons of METRIC and EC ETa at the four sites of eastern Washington State for five crops (winter wheat, spring garbanzo, spring canola, spring barley, and spring pea) by khan et al. [67] showed reasonable agreement, with an RMSE of 0.4 mm/d on satellite overpass days. Ortega-Salazar et al. [55] used the METRIC model to invert evapotranspiration in drip-irrigated olive orchards, and their RMSE for daily ET_a was 0.42 mm/day.

The acquisition of daily ET_a data is limited to sunny days with satellite overpasses, and such data are insufficient for a complete representation of the process during the entire growth period. Therefore, the cubic B-spline method was needed to extend the ET_rF available during the maize reproductive period to the entire reproductive period. The interpolation results reveal that the ET_rF curves for most years in Figure 7a–e are consistent with previous maize-related monitoring studies [68]. Unfortunately, the disadvantage of a small amount of image data is that it is difficult to overcome because of the single source of remote sensing image data. The lack of high-quality remote sensing images with few clouds in May 2014 and 2015 is more critical in the growth stage, leading to the ET_rF interpolation curve pattern of the corresponding years being less consistent with other images.

However, remote sensing data were still effective in qualitatively describing the ET_a trends of maize in most years. Ground measurements of *LAI* (Figure 5) indicated that maize under the DI treatment reached peak growth earlier than that of BI. As it was not possible to measure the *LAI* of maize during the initial growth stage, it was deduced from the maize growth that LAI_{DI} was greater than LAI_{BI} until May. Figure 6 shows that *LE* had a positive correlation with *LAI*, and that a high *LAI* value caused a higher *LE* value, which in turn affected the value of ET_a. Therefore, except for 2017, the ET_rF under the DI treatment was always higher than that under the BI treatment in the initial stage of maize growth in other years. The ET_rF curve also reflects the disease infestation of corn under DI in 2017, which is in clear contrast to other years when the ET_a of DI was higher than that of BI.

Previous studies have concluded that drip irrigation saves water and improves water use efficiency, primarily by reducing soil evaporation, compared to other irrigation methods. Traditional irrigation methods such as border irrigation may lead to high soil evaporation rather than crop transpiration, resulting in high evapotranspiration, which masks the potential water stress of the crop throughout the growth cycle [69,70]. However, asynchrony in the timing of the two irrigation operations in the study would increase soil evaporation from the farmland at different time periods, resulting in ET_a from the farmland that can sometimes be inconsistent with maize growth. In addition, as maize grows, the crop has

almost 100% leaf cover and no bare soil, narrowing the differences in ET_a between the two irrigation methods. Both irrigation methods followed the local production pattern, and irrigation scheduling was optimal. Consequently, it is difficult to distinguish between the two irrigation methods using only the daily ET_a obtained from satellite remote sensing data. There was also an uncertain relationship between the two ET_rF curves after interpolation. Based on the available data or curves, it is not possible to intuitively determine which irrigation method consumes more water. Therefore, it is necessary to extend the ET_a of the two maize farmlands over the entire growth stages and continue to explore the differences in the ET_a of seed maize under the two irrigation methods.

The trend In ET_a over time was distinct for maize, with clear boundaries between the different farmlands. Combined with the vegetation distribution in Figure 8, there were no ET_a anomalies in the farmlands of the same crop (Figure 9), confirming the suitability of the spatial distribution of ET_a obtained from the estimation. At the beginning of maize growth (May), the ET_a for maize croplands was below 3 mm/day under both irrigation methods. When maize was rapidly growing, such as on 10 and 26 June ($NDVI_{DM}$ = 0.39, 0.76, $NDVI_{BM}$ = 0.28, 0.64, respectively, shown Figure 8), combined with the *NDVI* of the crop growth process, the growth of seed maize under DI was better than under BI. Therefore, the ET_a of DI during the fast growth stage of maize was higher than that of BI. In the middle and late stages of maize growth (July 12 and 21 and August 22), as shown in Figure 7, the ET_a of BI was slightly higher than that of DI (ET_{DI} = 6.99, 6.54, and 5.31 mm; ET_{BI} = 7.49, 6.80, and 5.45 mm). The inspection of vegetation in the two fields ($NDVI_{DI}$ = 0.75, 0.71, and 0.68; $NDVI_{BI}$ = 0.80, 0.77, and 0.76) showed that the growth of BI maize was better than that of DI maize. Combined with previous studies, DI accelerated maize growth and shortened the entire experimental period [38,39]. Therefore, it is reasonable that DI maize enters the decline stage earlier, and its ET_a is lower than that for BI maize.

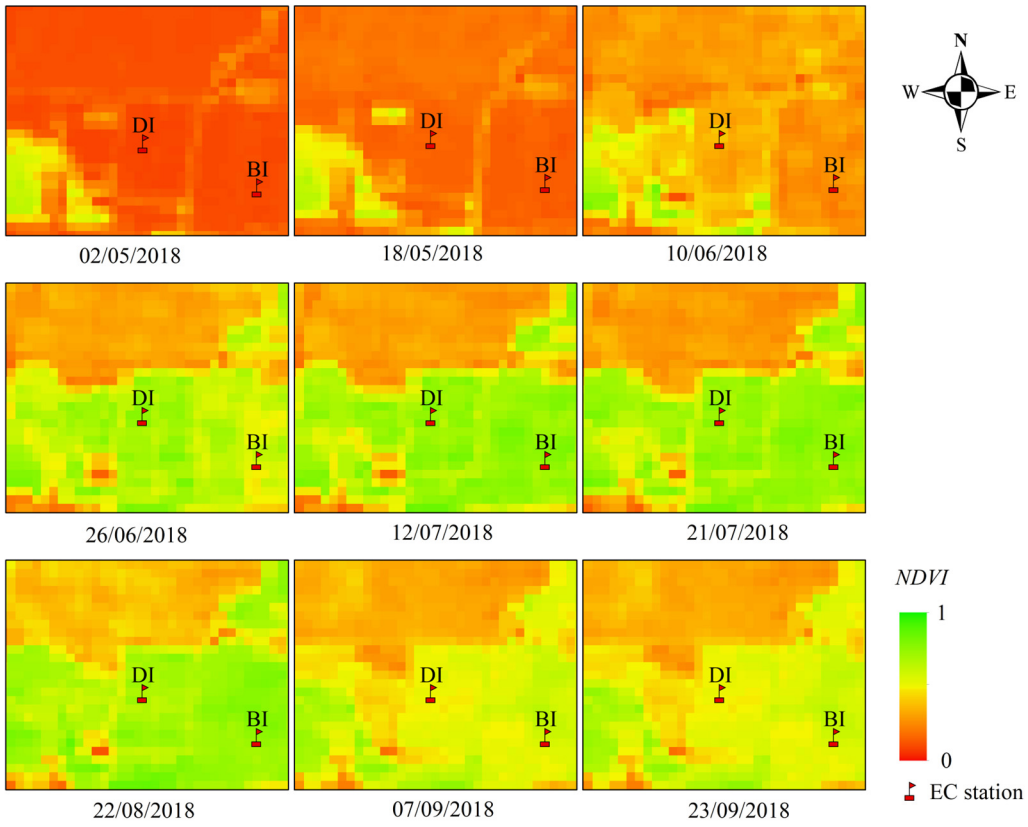

Figure 8. Spatial and temporal variability of *NDVI* on satellite overpass days at three observation sites in 2018. *NDVI* is the normalized difference vegetation index. DI is the drip irrigation method. BI is the border irrigation method. EC is the eddy covariance method.

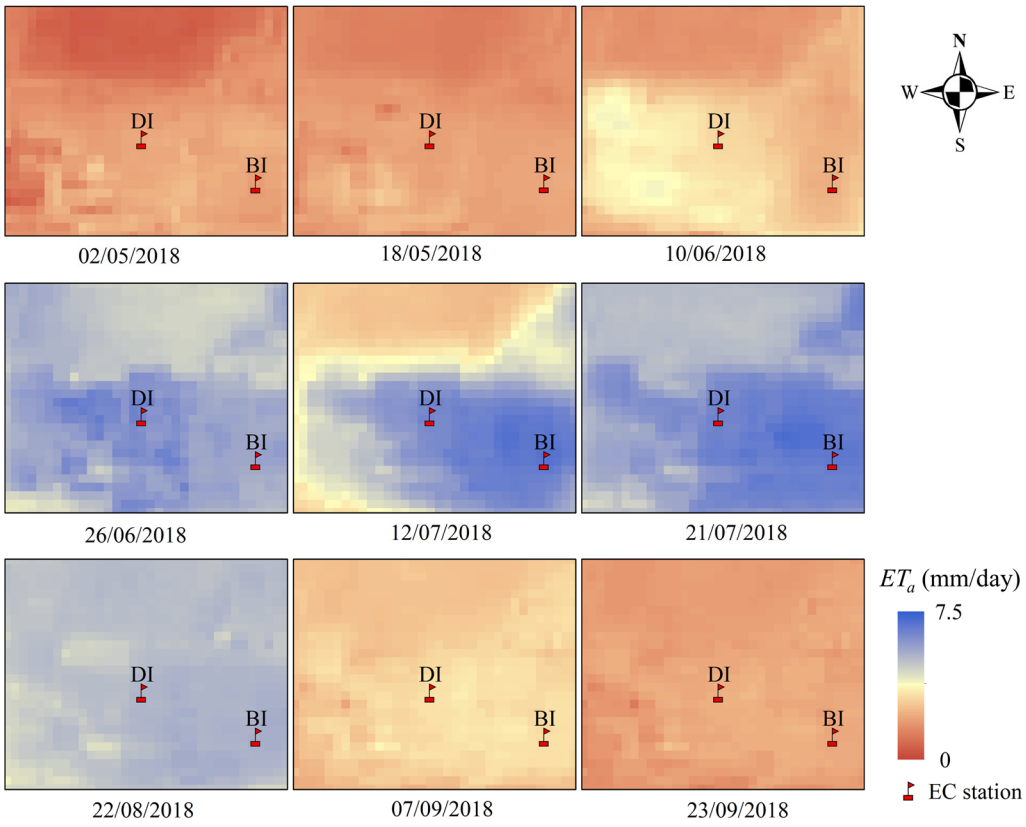

Figure 9. Spatial and temporal variation of the daily satellite overpass ET_a in the three observation sites in 2018. ET_a (mm/day) is the actual daily evapotranspiration. DI is the drip irrigation method. BI is the border irrigation method. EC is the eddy covariance method.

4.3. Differences in the Growth Stage and Irrigation Methods of ET_a

Figure 10 shows a comparison of the ET_a estimated by the METRIC model for each growth stage with the ET_a obtained from the other observations. After the expansion of daily ET_a using the Cubic B-Spline method, the sum of each growth stage was determined and compared with three observations (water balance, Bowen ratio, and EC system, with light-to-dark border colors). For this petal map, the more uniform the petal lengths of the same color, the higher the consistency of the four methods of obtaining ET_a, and the better the accuracy of the estimates. In the same year, ET_a fluctuated with changes in growth stages. Using the extended model on the time scale with EC observations as validation values, the ET_a estimates for the different growth stages of maize were accurate, with the worst Bias occurring during the shooting (yellow bars) period ($Bias_{BI}$ = 15.37 mm, $Bias_{DI}$ = 7.90 mm). Maize growth during the shooting stage is very fast and cannot be accurately represented when there are few satellite remote sensing images. Due to the limited amount of data provided by remote sensing images, estimates can only be obtained based on the overall trend of rapidly growing maize. This shortcoming can be compensated for by increasing the temporal resolution of remote sensing data using methods such as data fusion. The time scale expansion for ET_a is only quantitatively represented and cannot demonstrate the spatial variability at times other than satellite overpass days. Therefore, further in-depth studies are needed to analyze the spatial variability of ET_a at different growth stages and its relationship with precipitation.

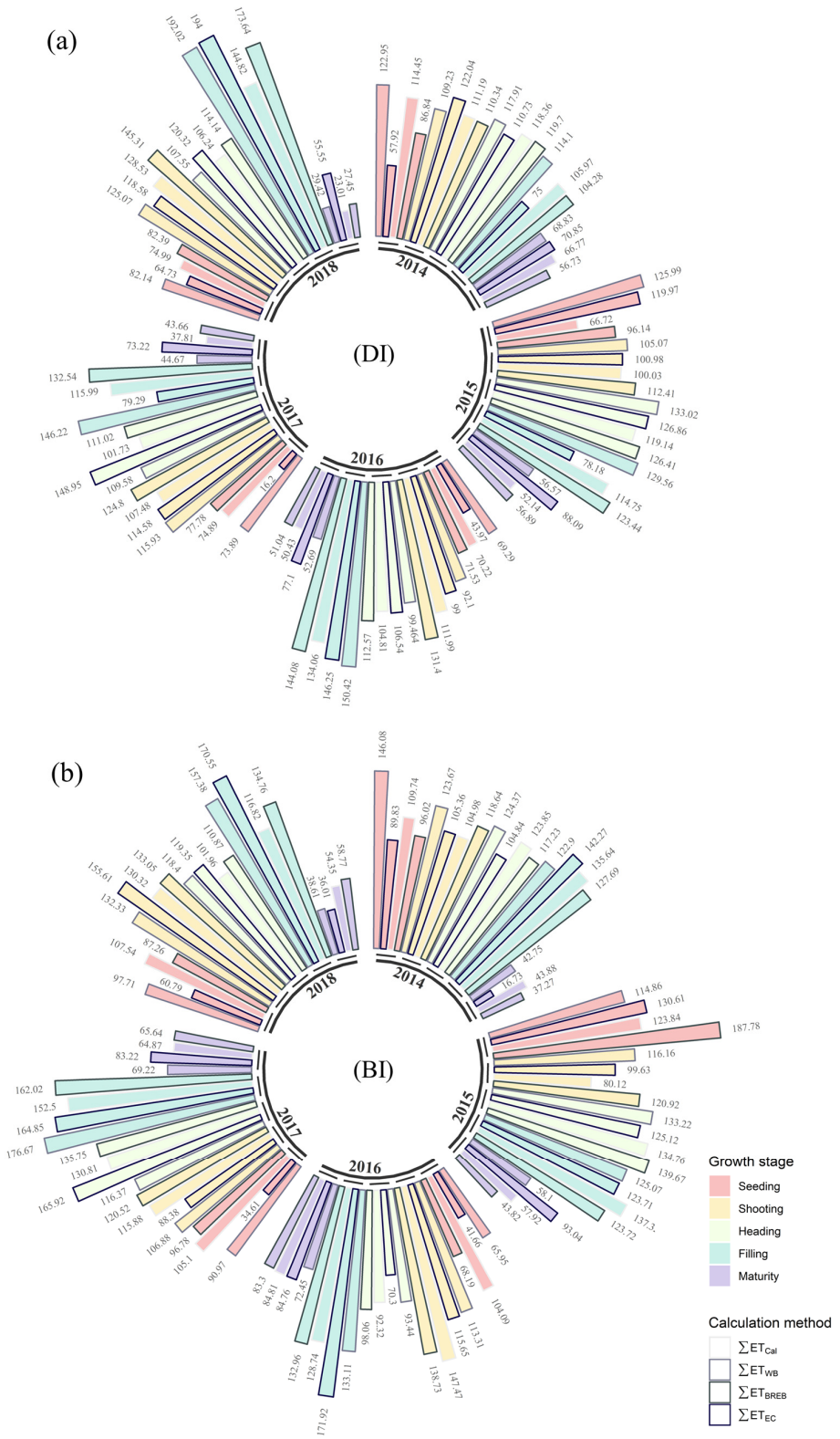

Figure 10. Histogram of estimated ET_a versus three observations for the five growth stages of maize (2014–2018) under DI (**a**) and BI (**b**). DI is the drip irrigation method. BI is the border irrigation method. ΣET is the actual evapotranspiration in each stage of growth of maize. Cal, WB, BREB, and EC (calculation using remote sensing model, water balance, Bowen ratio and energy balance method, and eddy covariance method) are the methods of actual evapotranspiration.

The average daily ET_a was calculated based on the number of days and time scale extensions in each growth stage, and then the calculated ET_a was compared with the three observations. The indicators (R^2 and RMSE) between the estimated and measured ET_a showed high accuracy for most cases (Figure 11). However, the difference between the ET_a average obtained from remote sensing estimates and the WB data was extensive and performed poorly in most years. The ET_a obtained from the WB method at the seeding stage was much lower than that obtained from the other observation data, as seen from the ET_a distribution at each growth stage in Figure 10b for 2017. The soil moisture content at seedling and maturity is low, but the measurement errors are high. Figure 11 shows the average daily ET_a at each growth stage for validation, amplifying the impact of ET_a at the seedling stage, which accounted for a smaller proportion of the total period. Using the BREB and EC observations for validation, the errors in the remote sensing estimates were small, with R^2 (red and green hollow symbols) greater than 0.7 and RMSE (red and green solid symbols) less than 0.6 mm/day for both irrigation methods over five years.

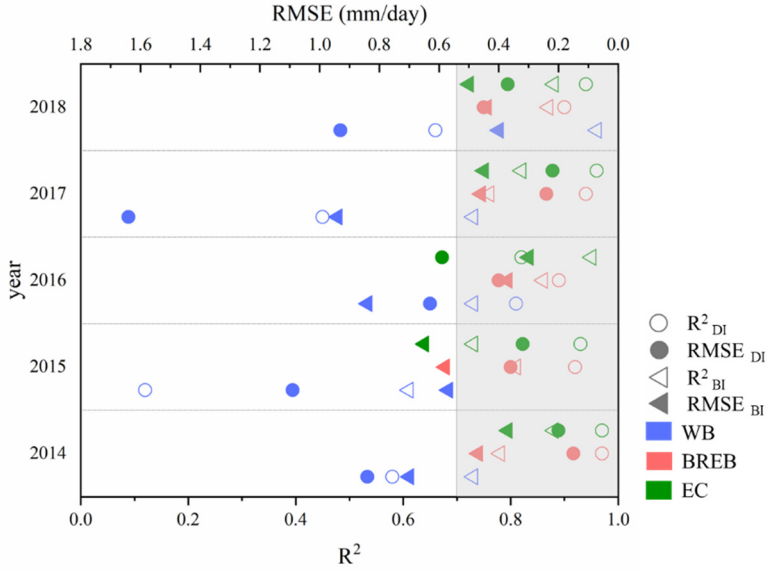

Figure 11. Accuracy of the estimated daily average evapotranspiration using remote sensing models under two irrigation methods in different years compared to three observation methods. R^2 is the coefficient of determination. RMSE is the root mean square error (mm/day); DI is the drip irrigation method. BI is the border irrigation method. WB, BREB, and EC (water balance, Bowen ratio and energy balance method, and eddy covariance method) are the methods of ETa observation.

The results of the model for estimating water consumption in maize fields were highly accurate. Therefore, we expected to discriminate field differences between the two irrigation methods (drip vs. border). However, on satellite overpass days, ET_a was related to the change in surface soil water content caused by irrigation, and the difference in daily ET_a between the two irrigation methods could not be distinguished. The whole crop season ET_a was calculated, and the differences in the total ET_a under the two irrigation methods are shown in Figure 12. The timing of the satellite overpass was irregular for the entire maize growing period, owing to clouds. Therefore, this failed to reflect the effect on ET_a when BI soil evaporation was higher. Combined with the trend of the curves in Figure 7b, it was found that the ET_a of BI obtained after interpolating the satellite overpass time in 2015 was always smaller than the ET_a of DI in that year. The ET_a of BI maize cropland in other years was higher than DI maize cropland, which was consistent with the observed data. The differences in ET_a under the two irrigation methods obtained using the three methods observed in 2018 were inconsistent, but their mean values were consistent with the model estimates ($\Sigma ET_{BI} > \Sigma ET_{DI}$). It is clear from the above that the remote sensing evapotranspiration model is a reliable method for estimating ET_a when image

conditions permit it. For example, Semmens et al. [71] used a multi-sensor satellite data fusion approach combined with a two-source energy balance (TSEB)-based *ET* algorithm (Atmosphere–Land Exchange Inverse (ALEXI)) in Sacramento and San Joaquin counties, California, USA, to produce estimates of daily ET_a that were consistent with ground-based flux measurements for two neighboring Pinot Noir vineyards of different ages (with relative mean absolute errors in the order of 19–23% and an RMSE of about 1 mm/d).

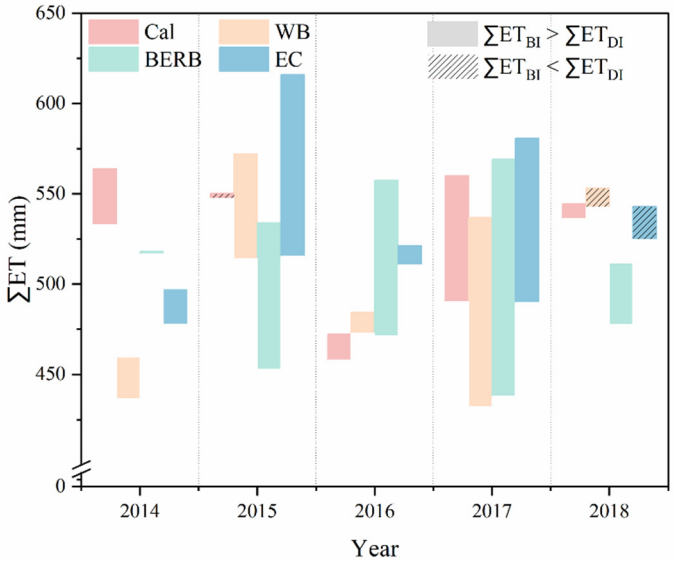

Figure 12. Differences in actual total evapotranspiration of maize during the growing season under the two irrigation methods. DI is the drip irrigation method. BI is the border irrigation method; ΣET (mm) is the actual evapotranspiration of the growing period of maize. Cal, WB, BREB, and EC (calculation using a remote sensing model, water balance, Bowen ratio and energy balance method, and eddy covariance method) are the methods used to obtain actual evapotranspiration.

5. Summary and Conclusions

Previous studies have focused only on the accuracy of the METRIC model to estimate SEBCs or ET_a for one or a few crops in a specific region. However, the reliability of the METRIC model was verified, and a new direction for its application should be explored. Therefore, in this study, we hope to use a remote sensing evapotranspiration model to obtain the regional ET_a and further understand whether it can be used to distinguish the differences in evapotranspiration among different irrigation methods.

This study used T_a obtained from a regression model to estimate R_n, which improved its accuracy. The estimation accuracy of *LE* from the METRIC model showed good performance (R^2 and RMSE were 0.88 and 42.44 W/m^2, respectively), which verified the applicability of the model in Northwest China. Good results were also obtained in estimating the SEBCs and ET_a from farmland at different timescales. The total accuracy of the ET_a estimation on the five-year overpass day of maize farmland reached R^2 = 0.93 and RMSE = 0.48 mm. When the anomaly was removed in 2015, the 4-year average ET_a of maize was 31 mm lower for DI than for BI, with the mean value of the three observations being 40 mm. The model has a high discriminative ability for maize under different irrigation methods, expanding the application scope of the satellite remote sensing evapotranspiration model.

The maize observation sites in this study were similar to most local farmlands and were managed with high water and fertilizer. The METRIC model was shown to have the ability to distinguish ET_a differences between different irrigation methods and is a powerful tool for the large-scale demonstration of the changes in and impacts of water-saving irrigation on conventional irrigation. We also believe that a higher precision ET_a dataset for maize fields is reliable support for the further monitoring of crop growth and yield. Although the current limitations of the spatial and temporal resolution of satellite

remote sensing data do not allow for the monitoring of changes in irrigation within plots, total water use calculations over the maize growth cycle show good results, which is very beneficial for regional water managers to plan and schedule agricultural water use. This is a good starting point and evidence for the application of satellite remote sensing technology to distinguish regional-scale farmland management measures and is expected to be applied to high-precision farmland management with the support of remote sensing data quality and quantity.

Author Contributions: Conceptualization, Y.L.; methodology, Y.L. and S.O.-F.; software, Y.L.; validation, Y.F, Y.H. and Y.L.; formal analysis, Y.L. and S.W.; investigation, W.Y.; resources, S.L.; data curation, S.L. and Y.L.; writing—original draft preparation, Y.L.; writing—review and editing, Y.L., Y.F., Y.H. and S.W.; visualization, Y.L. and W.Y.; supervision, W.Y., F.T. and S.W.; project administration, S.O.-F. and S.W.; funding acquisition, S.O.-F. and S.W. All authors have read and agreed to the published version of the manuscript.

Funding: This research was funded by the International and regional cooperation and exchange projects of the National Natural Science Foundation of China (51961125205), the National Key R&D Program of China (2022YFD1900401), and the Chilean government through National Agency for Research and Development (ANID)/PCI (NSFC190013).

Data Availability Statement: The data sources used in this study are greatly appreciated. Landsat 8 satellite remote sensing and digital elevation model (DEM) data were provided by the Google Earth Engine (GEE) platform (https://earthengine.google.com/ (accessed on 25 December 2023)). Meteorological data were obtained from the National Meteorological Information Center (http://data.cma.cn/ (accessed on 25 December 2023)). Ground observation data were provided by the National Field Scientific Observation and Research Station on Efficient Water Use of Oasis Agriculture in Wuwei of Gansu Province. This study is available on request from the corresponding author.

Conflicts of Interest: The authors declare no conflicts of interest.

Appendix A

Table A1. Definition of variables in the METRIC model.

Symbol	Definition	Unit/Constant
C_p	Air heat constant	1004 J/kg/K
ET_{daily_i}	Evapotranspiration value on the i day	mm
ET_{daily}	Ratio of actual to reference evapotranspiration	mm
ET_{inst}	Instantaneous evapotranspiration	mm/h
$ET_{overpass}$	Instantaneous evapotranspiration at overpass time from satellite	Mm/h
ET_rF	Ratio of actual to reference evapotranspiration	/
ET_{r_hourly}	Instantaneous reference evapotranspiration	mm
ET_{total}	Total water consumption during the growing period	mm
G_{SC}	Solar constant	1367 W/m^2
$R_L \uparrow$	Outgoing long-wave radiation	W/m^2
$R_L \downarrow$	Incoming long-wave incidence	W/m^2
R_S	Surface incident short-wave radiation	W/m^2
R_n	Net radiation flux	W/m^2
T_s	Surface temperature	K
T_a	Near-surface air temperature	K
d_r	Relative Earth–Sun distance	/
r_{ah}	Aerodynamic resistance	s/m
ε_s	Surface emissivity	/
ρ_{air}	Air density	1.293 kg/m^3
G	Soil and water flux heat	W/m^2
H	Sensible heat flux	W/m^2
LE	Latent heat flux	W/m^2

Table A1. *Cont.*

Symbol	Definition	Unit/Constant
N	Time interval between sunrise and sunset	h
dT	Temperature difference between the height Z_1 of the ground and the reference height Z_2 of 2 m	k
U^*	Friction velocity	m/s
i	Number of days in the growing period	/
t	Satellite overpass time	/
z	Local altitude	m
θ	Solar incident angle	rad
λ	Latent heat of water vaporization	J/kg
σ	Stefan–Boltzman constant	5.67×10^{-8} W/m^2/K^4

References

1. Su, Z. The Surface Energy Balance System (SEBS) for Estimation of Turbulent Heat Fluxes. *Hydrol. Earth Syst. Sci.* **2002**, *6*, 85–99. [CrossRef]
2. Byun, K.; Liaqat, U.W.; Choi, M. Dual-Model Approaches for Evapotranspiration Analyses over Homo- and Heterogeneous Land Surface Conditions. *Agric. For. Meteorol.* **2014**, *197*, 169–187. [CrossRef]
3. Sauer, T.J.; Hatfield, J.L.; Prueger, J.H.; Norman, J.M. Surface Energy Balance of a Corn Residue-Covered Field. *Agric. For. Meteorol.* **1998**, *89*, 155–168. [CrossRef]
4. Wang, X.; Huo, Z.; Shukla, M.K.; Wang, X.; Guo, P.; Xu, X. Energy Fl Uxes and Evapotranspiration over Irrigated Maize Fi Eld in an Arid Area with Shallow Groundwater. *Agric. Water Manag.* **2020**, *228*, 105922. [CrossRef]
5. Bi, W.; Weng, B.; Yan, D.; Wang, M.; Wang, H.; Wang, J.; Yan, H. Effects of Drought-Flood Abrupt Alternation on Phosphorus in Summer Maize Farmland Systems. *Geoderma* **2020**, *363*, 114147. [CrossRef]
6. He, L.; Bao, J.; Daccache, A.; Wang, S.; Guo, P. Optimize the Spatial Distribution of Crop Water Consumption Based on a Cellular Automata Model: A Case Study of the Middle Heihe River Basin, China. *Sci. Total Environ.* **2020**, *720*, 137569. [CrossRef]
7. Turral, H.; Burke, J.; Faures, J.M.; Faures, J.M. *Climate Change, Water and Food Security*; Food and Agriculture Organization of the United Nations: Rome, Italy, 2011; p. 204.
8. WWAP (United Nations World Water Assessment Programme)/UN-Water. *The United Nations World Water Development Report 2018: Nature-Based Solutions for Water*; UN-Water: Geneva, Switzerland, 2018; ISBN 9789231002649. Available online: https://www.unwater.org/publications/world-water-development-report-2018 (accessed on 25 December 2023).
9. Kang, S.; Hao, X.; Du, T.; Tong, L.; Su, X.; Lu, H.; Li, X.; Huo, Z.; Li, S.; Ding, R. Improving Agricultural Water Productivity to Ensure Food Security in China under Changing Environment: From Research to Practice. *Agric. Water Manag.* **2017**, *179*, 5–17. [CrossRef]
10. Huang, Y.; Li, Y.P.; Chen, X.; Ma, Y.G. Optimization of the Irrigation Water Resources for Agricultural Sustainability in Tarim River Basin, China. *Agric. Water Manag.* **2012**, *107*, 74–85. [CrossRef]
11. Vörösmarty, C.J.; Federer, C.A.; Schloss, A.L. Potential Evaporation Functions Compared on US Watersheds: Possible Implications for Global-Scale Water Balance and Terrestrial Ecosystem Modeling. *J. Hydrol.* **1998**, *207*, 147–169. [CrossRef]
12. Kite, G. Using a Basin-Scale Hydrological Model to Estimate Crop Transpiration and Soil Evaporation. *J. Hydrol.* **2000**, *229*, 59–69. [CrossRef]
13. Senay, G.B.; Budde, M.E.; Verdin, J.P. Enhancing the Simplified Surface Energy Balance (SSEB) Approach for Estimating Landscape ET: Validation with the METRIC Model. *Agric. Water Manag.* **2011**, *98*, 606–618. [CrossRef]
14. De C. Teixeira, A.H.; Bastiaanssen, W.G.M.; Ahmad, M.D.; Bos, M.G. Reviewing SEBAL Input Parameters for Assessing Evapotranspiration and Water Productivity for the Low-Middle São Francisco River Basin, Brazil. Part A: Calibration and Validation. *Agric. For. Meteorol.* **2009**, *149*, 462–476. [CrossRef]
15. Wetzel Seemann, S.; Li, J.; Gumley, L.E.; Strabala, K.I.; Menzel, W.P. Operational Retrieval of Atmospheric Temperature, Moisture, and Ozone from MODIS Infrared Radiances. *Appl. Weather Satell.* **2003**, *4895*, 168. [CrossRef]
16. Zamani Losgedaragh, S.; Rahimzadegan, M. Evaluation of SEBS, SEBAL, and METRIC Models in Estimation of the Evaporation from the Freshwater Lakes (Case Study: Amirkabir Dam, Iran). *J. Hydrol.* **2018**, *561*, 523–531. [CrossRef]
17. Xiang, K.; Li, Y.; Horton, R.; Feng, H. Similarity and Difference of Potential Evapotranspiration and Reference Crop Evapotranspiration—A Review. *Agric. Water Manag.* **2020**, *232*, 106043. [CrossRef]
18. Douglas, E.M.; Jacobs, J.M.; Sumner, D.M.; Ray, R.L. A Comparison of Models for Estimating Potential Evapotranspiration for Florida Land Cover Types. *J. Hydrol.* **2009**, *373*, 366–376. [CrossRef]
19. Srivastava, A.; Sahoo, B.; Raghuwanshi, N.S.; Singh, R. Evaluation of Variable-Infiltration Capacity Model and MODIS-Terra Satellite-Derived Grid-Scale Evapotranspiration Estimates in a River Basin with Tropical Monsoon-Type Climatology. *J. Irrig. Drain. Eng.* **2017**, *143*, 04017028. [CrossRef]

20. Adamala, S.; Raghuwanshi, N.S.; Mishra, A.; Tiwari, M.K. Evapotranspiration Modeling Using Second-Order Neural Networks. *J. Hydrol. Eng.* **2014**, *19*, 1131–1140. [CrossRef]
21. Peng, L.; Li, Y.; Feng, H. The Best Alternative for Estimating Reference Crop Evapotranspiration in Different Sub-Regions of Mainland China. *Sci. Rep.* **2017**, *7*, 5458. [CrossRef]
22. Mokhtari, A.; Noory, H.; Pourshakouri, F.; Haghighatmehr, P.; Afrasiabian, Y.; Razavi, M.; Fereydooni, F.; Sadeghi Naeni, A. Calculating Potential Evapotranspiration and Single Crop Coefficient Based on Energy Balance Equation Using Landsat 8 and Sentinel-2. *ISPRS J. Photogramm. Remote Sens.* **2019**, *154*, 231–245. [CrossRef]
23. Alberto, M.C.R.; Quilty, J.R.; Buresh, R.J.; Wassmann, R.; Haidar, S.; Correa, T.Q.; Sandro, J.M. Actual Evapotranspiration and Dual Crop Coefficients for Dry-Seeded Rice and Hybrid Maize Grown with Overhead Sprinkler Irrigation. *Agric. Water Manag.* **2014**, *136*, 1–12. [CrossRef]
24. Garrido-Rubio, J.; Calera, A.; Arellano, I.; Belmonte, M.; Fraile, L.; Ortega, T.; Bravo, R.; González-Piqueras, J. Evaluation of Remote Sensing-Based Irrigation Water Accounting at River Basin District Management Scale. *Remote Sens.* **2020**, *12*, 3187. [CrossRef]
25. Paço, T.A.; Pôças, I.; Cunha, M.; Silvestre, J.C.; Santos, F.L.; Paredes, P.; Pereira, L.S. Evapotranspiration and Crop Coefficients for a Super Intensive Olive Orchard. An Application of SIMDualKc and METRIC Models Using Ground and Satellite Observations. *J. Hydrol.* **2014**, *519*, 2067–2080. [CrossRef]
26. Bastiaanssen, W.G.M.; Noordman, E.J.M.; Pelgrum, H.; Davids, G.; Thoreson, B.P.; Allen, R.G. SEBAL Model with Remotely Sensed Data to Improve Water-Resources Management under Actual Field Conditions. *J. Irrig. Drain. Eng.* **2005**, *131*, 85–93. [CrossRef]
27. Paul, G.; Gowda, P.H.; Vara Prasad, P.V.; Howell, T.A.; Aiken, R.M.; Neale, C.M.U. Investigating the Influence of Roughness Length for Heat Transport (Zoh) on the Performance of SEBAL in Semi-Arid Irrigated and Dryland Agricultural Systems. *J. Hydrol.* **2014**, *509*, 231–244. [CrossRef]
28. Liaqat, U.W.; Choi, M. Surface Energy Fluxes in the Northeast Asia Ecosystem: SEBS and METRIC Models Using Landsat Satellite Images. *Agric. For. Meteorol.* **2015**, *214–215*, 60–79. [CrossRef]
29. French, A.N.; Hunsaker, D.J.; Thorp, K.R. Remote Sensing of Environment Remote Sensing of Evapotranspiration over Cotton Using the TSEB and METRIC Energy Balance Models. *Remote Sens. Environ.* **2015**, *158*, 281–294. [CrossRef]
30. Elnmer, A.; Khadr, M.; Kanae, S.; Tawfik, A. Mapping Daily and Seasonally Evapotranspiration Using Remote Sensing Techniques over the Nile Delta. *Agric. Water Manag.* **2019**, *213*, 682–692. [CrossRef]
31. Allen, R.G.; Tasumi, M.; Morse, A.; Trezza, R.; Wright, J.L.; Bastiaanssen, W.; Kramber, W.; Lorite, I.; Robison, C.W. Satellite-Based Energy Balance for Mapping Evapotranspiration with Internalized Calibration (METRIC)—Applications. *J. Irrig. Drain. Eng.* **2007**, *133*, 395–406. [CrossRef]
32. Bastiaanssen, W.G.M.; Menenti, M.; Feddes, R.A.; Holtslag, A.A.M. A Remote Sensing Surface Energy Balance Algorithm for Land (SEBAL). 1. Formulation. *J. Hydrol.* **1998**, *212–213*, 198–212. [CrossRef]
33. Allen, R.; Irmak, A.; Trezza, R.; Hendrickx, J.M.H.; Bastiaanssen, W.; Kjaersgaard, J. Satellite-Based ET Estimation in Agriculture Using SEBAL and METRIC. *Hydrol. Process.* **2011**, *25*, 4011–4027. [CrossRef]
34. Allen, R.G.; Burnett, B.; Kramber, W.; Huntington, J.; Kjaersgaard, J.; Kilic, A.; Kelly, C.; Trezza, R. Automated Calibration of the METRIC-Landsat Evapotranspiration Process. *J. Am. Water Resour. Assoc.* **2013**, *49*, 563–576. [CrossRef]
35. Trezza, R.; Allen, R.G.; Tasumi, M. Estimation of Actual Evapotranspiration along the Middle Rio Grande of New Mexico Using MODIS and Landsat Imagery with the METRIC Model. *Remote Sens.* **2013**, *5*, 5397–5423. [CrossRef]
36. Choi, M.; Kustas, W.P.; Anderson, M.C.; Allen, R.G.; Li, F.; Kjaersgaard, J.H. An Intercomparison of Three Remote Sensing-Based Surface Energy Balance Algorithms over a Corn and Soybean Production Region (Iowa, U.S.) during SMACEX. *Agric. For. Meteorol.* **2009**, *149*, 2082–2097. [CrossRef]
37. Nisa, Z.; Khan, M.S.; Govind, A.; Marchetti, M.; Lasserre, B.; Magliulo, E.; Manco, A. Evaluation of SEBS, METRIC-EEFlux, and QWaterModel Actual Evapotranspiration for a Mediterranean Cropping System in Southern Italy. *Agronomy* **2021**, *11*, 345. [CrossRef]
38. Wang, Y.; Li, S.; Qin, S.; Guo, H.; Yang, D.; Lam, H.M. How Can Drip Irrigation Save Water and Reduce Evapotranspiration Compared to Border Irrigation in Arid Regions in Northwest China. *Agric. Water Manag.* **2020**, *239*, 106256. [CrossRef]
39. Qin, S.; Li, S.; Kang, S.; Du, T.; Tong, L.; Ding, R. Can the Drip Irrigation under Film Mulch Reduce Crop Evapotranspiration and Save Water under the Sufficient Irrigation Condition? *Agric. Water Manag.* **2016**, *177*, 128–137. [CrossRef]
40. Gao, L.; Kang, S.; Bai, X.; Li, S.; Niu, J.; Ding, R. Water-Carbon Relationships and Variations from the Canopy to Ecosystem Scale in a Sparse Vineyard in the Northwest China. *J. Hydrol.* **2021**, *600*, 126469. [CrossRef]
41. Becker, W.R.; Ló, T.B.; Johann, J.A.; Mercante, E. Statistical Features for Land Use and Land Cover Classification in Google Earth Engine. *Remote Sens. Appl. Soc. Environ.* **2021**, *21*, 100459. [CrossRef]
42. Li, S.; Zhang, L.; Kang, S.; Tong, L.; Du, T.; Hao, X.; Zhao, P. Comparison of Several Surface Resistance Models for Estimating Crop Evapotranspiration over the Entire Growing Season in Arid Regions. *Agric. For. Meteorol.* **2015**, *208*, 1–15. [CrossRef]
43. Li, S.; Kang, S.; Zhang, L.; Zhang, J. On the Attribution of Changing Crop Evapotranspiration in Arid Regions Using Four Methods. *J. Hydrol.* **2018**, *563*, 576–585. [CrossRef]

44. Bowen, I.S. The Ratio of Heat Losses by Conduction and by Evaporation from Any Water Surface. *Phys. Rev.* **1926**, *27*, 779–787. [CrossRef]
45. Perez, P.J.; Castellvi, F.; Ibañez, M.; Rosell, J.I. Assessment of Reliability of Bowen Ratio Method for Partitioning Fluxes. *Agric. For. Meteorol.* **1999**, *97*, 141–150. [CrossRef]
46. Baldocchi, D.D. Assessing the Eddy Covariance Technique for Evaluating Carbon Dioxide Exchange Rates of Ecosystems: Past, Present and Future. *Glob. Chang. Biol.* **2003**, *9*, 479–492. [CrossRef]
47. Shuttleworth, W.J. Putting the "vap" into Evaporation. *Hydrol. Earth Syst. Sci.* **2007**, *11*, 210–244. [CrossRef]
48. Li, Z.L.; Tang, R.; Wan, Z.; Bi, Y.; Zhou, C.; Tang, B.; Yan, G.; Zhang, X. A Review of Current Methodologies for Regional Evapotranspiration Estimation from Remotely Sensed Data. *Sensors* **2009**, *9*, 3801–3853. [CrossRef]
49. Windahl, E.; de Beurs, K. An Intercomparison of Landsat Land Surface Temperature Retrieval Methods under Variable Atmospheric Conditions Using in Situ Skin Temperature. *Int. J. Appl. Earth Obs. Geoinf.* **2016**, *51*, 11–27. [CrossRef]
50. Chen, F.; Liu, Y.; Liu, Q.; Qin, F. A Statistical Method Based on Remote Sensing for the Estimation of Air Temperature in China. *Int. J. Climatol.* **2015**, *35*, 2131–2143. [CrossRef]
51. Liu, Y.; Ortega-Farías, S.; Tian, F.; Wang, S.; Li, S. Estimation of Surface and Near-Surface Air Temperatures in Arid Northwest China Using Landsat Satellite Images. *Front. Environ. Sci.* **2021**, *9*, 609. [CrossRef]
52. Flood, N. Continuity of Reflectance Data between Landsat-7 ETM+ and Landsat-8 OLI, for Both Top-of-Atmosphere and Surface Reflectance: A Study in the Australian Landscape. *Remote Sens.* **2014**, *6*, 7952–7970. [CrossRef]
53. Liang, S. Narrowband to Broadband Conversions of Land Surface Albedo I. *Remote Sens. Environ.* **2001**, *76*, 213–238. [CrossRef]
54. Allen, R.G.; Tasumi, M.; Trezza, R. Satellite-Based Energy Balance for Mapping Evapotranspiration with Internalized Calibration (METRIC)—Model. *J. Irrig. Drain. Eng.* **2007**, *133*, 380–394. [CrossRef]
55. Ortega-Salazar, S.; Ortega-Farías, S.; Kilic, A.; Allen, R. Performance of the METRIC Model for Mapping Energy Balance Components and Actual Evapotranspiration over a Superintensive Drip-Irrigated Olive Orchard. *Agric. Water Manag.* **2021**, *251*, 106861. [CrossRef]
56. Bastiaanssen, W.G.M. SEBAL-Based Sensible and Latent Heat Fluxes in the Irrigated Gediz Basin, Turkey. *J. Hydrol.* **2000**, *229*, 87–100. [CrossRef]
57. Numata, I.; Khand, K.; Kjaersgaard, J.; Cochrane, M.A.; Silva, S.S. Evaluation of Landsat-Based Metric Modeling to Provide High-Spatial Resolution Evapotranspiration Estimates for Amazonian Forests. *Remote Sens.* **2017**, *9*, 46. [CrossRef]
58. Tayebi, S.; Momani, S.; Abu, O. The Cubic B-Spline Interpolation Method for Numerical Point Solutions of Conformable Boundary Value Problems. *Alex. Eng. J.* **2022**, *61*, 1519–1528. [CrossRef]
59. Oliveira, B.S.; Moraes, E.C.; Carrasco-Benavides, M.; Bertani, G.; Mataveli, G.A.V. Improved Albedo Estimates Implemented in the METRIC Model for Modeling Energy Balance Fluxes and Evapotranspiration over Agricultural and Natural Areas in the Brazilian Cerrado. *Remote Sens.* **2018**, *10*, 1181. [CrossRef]
60. Carrasco-Benavides, M.; Ortega-Farías, S.; Lagos, L.O.; Kleissl, J.; Morales-Salinas, L.; Kilic, A. Parameterization of the Satellite-Based Model (METRIC) for the Estimation of Instantaneous Surface Energy Balance Components over a Drip-Irrigated Vineyard. *Remote Sens.* **2014**, *6*, 11342–11371. [CrossRef]
61. Feng, J.; Wang, W.; Che, T.; Xu, F. Performance of the Improved Two-Source Energy Balance Model for Estimating Evapotranspiration over the Heterogeneous Surface. *Agric. Water Manag.* **2023**, *278*, 108159. [CrossRef]
62. Ge, N.; Zhong, L.; Ma, Y.; Cheng, M.; Wang, X.; Zou, M.; Huang, Z. Estimation of Land Surface Heat Fluxes Based on Landsat 7 ETM+ Data and Field Measurements over the Northern Tibetan Plateau. *Remote Sens.* **2019**, *11*, 2899. [CrossRef]
63. Mutanga, O.; Skidmore, A.K. Narrow Band Vegetation Indices Overcome the Saturation Problem in Biomass Estimation. *Int. J. Remote Sens.* **2004**, *25*, 3999–4014. [CrossRef]
64. Kamyab, A.D.; Mokhtari, S.; Jafarinia, R. A Comparative Study in Quantification of Maize Evapotranspiration for Iranian Maize Farm Using SEBAL and METRIC-1 EEFLux Algorithms. *Acta Geophys.* **2022**, *70*, 319–332. [CrossRef]
65. Xue, J.; Bali, K.M.; Light, S.; Hessels, T.; Kisekka, I. Evaluation of Remote Sensing-Based Evapotranspiration Models against Surface Renewal in Almonds, Tomatoes and Maize. *Agric. Water Manag.* **2020**, *238*, 106228. [CrossRef]
66. Reyes-González, A.; Kjaersgaard, J.; Trooien, T.; Reta-Sánchez, D.G.; Sánchez-Duarte, J.I.; Preciado-Rangel, P.; Fortis-Hernández, M. Comparison of Leaf Area Index, Surface Temperature, and Actual Evapotranspiration Estimated Using the METRIC Model and In Situ Measurements. *Sensors* **2019**, *19*, 1857. [CrossRef] [PubMed]
67. Khan, A.; Stöckle, C.O.; Nelson, R.L.; Peters, T.; Adam, J.C.; Lamb, B.; Chi, J.; Waldo, S. Estimating Biomass and Yield Using Metric Evapotranspiration and Simple Growth Algorithms. *Agron. J.* **2019**, *111*, 536–544. [CrossRef]
68. Zhang, B.; Liu, Y.; Xu, D.; Zhao, N.; Lei, B.; Rosa, R.D.; Paredes, P.; Paço, T.A.; Pereira, L.S. The Dual Crop Coefficient Approach to Estimate and Partitioning Evapotranspiration of the Winter Wheat-Summer Maize Crop Sequence in North China Plain. *Irrig. Sci.* **2013**, *31*, 1303–1316. [CrossRef]
69. Zhang, T.; Zou, Y.; Kisekka, I.; Biswas, A.; Cai, H. Comparison of Different Irrigation Methods to Synergistically Improve Maize's Yield, Water Productivity and Economic Benefits in an Arid Irrigation Area. *Agric. Water Manag.* **2021**, *243*, 106497. [CrossRef]

70. Sandhu, O.S.; Gupta, R.K.; Thind, H.S.; Jat, M.L.; Sidhu, H.S. Yadvinder-Singh Drip Irrigation and Nitrogen Management for Improving Crop Yields, Nitrogen Use Efficiency and Water Productivity of Maize-Wheat System on Permanent Beds in North-West India. *Agric. Water Manag.* **2019**, *219*, 19–26. [CrossRef]
71. Semmens, K.A.; Anderson, M.C.; Kustas, W.P.; Gao, F.; Alfieri, J.G.; McKee, L.; Prueger, J.H.; Hain, C.R.; Cammalleri, C.; Yang, Y.; et al. Monitoring Daily Evapotranspiration over Two California Vineyards Using Landsat 8 in a Multi-Sensor Data Fusion Approach. *Remote Sens. Environ.* **2016**, *185*, 155–170. [CrossRef]